W.I. Beavers, D.E. Dudgeon, J.W. Beletic, and M.T. Lane

Speckle Imaging through the Atmosphere

The atmosphere is the limiting factor in high-resolution ground-based optical telescope observations of objects in space. New speckle-imaging techniques allow astronomers to overcome atmospheric distortion and achieve the goal of diffraction-limited ground-based telescope performance. Studies and experiments at Lincoln Laboratory utilize speckle imaging for observation of near-earth satellites. Thousands of separate exposures, each 2 to 5 ms in duration, are collected within a few seconds. A computationally intensive algorithm is then used to reconstruct a single diffraction-limited image from the collection of separate exposures. The image-reconstruction process effectively removes the distortion imposed by the atmosphere. Photon noise, which limits the quality of image reconstruction, must be properly compensated by the actual detector calibration.

A textbook prediction of telescope resolving power, or limiting detectable angular separation (between double stars, for example), rarely describes actual telescope performance. Theoretically, the smallest resolvable angle θ for a telescope with objective lens or mirror of diameter D, in visible light, is

$$\theta = \frac{0.12}{D}$$

where D is in meters and θ is in seconds of arc. If no atmosphere were present, θ would be the limit of resolution for any given telescope.

However, turbulence in the atmosphere causes a point of light in space, such as a star, to appear through telescopes on earth as a puffed image, or *seeing disk*. The turbulence at any instant produces variations in atmospheric density, temperature, and index of refraction. As an example, the seeing disk undergoes excursions or apparent rapid movement due to instantaneous tilts of the wavefronts reaching the telescope. Furthermore, the twinkling, or scintillation, of light, which is visible to the naked eye, occurs in the signal of any detector at the focal plane of the telescope. The twinkling represents changes in the instantaneous brightness of a star or point-source object at frequencies up to a few hundred hertz. The angular spread of the seeing disk, the wandering of the image, and the twinkling or scintillation are all consequences of the passage of the beam through the atmosphere.

Until recent years, attempts to overcome the problems in seeing were directed primarily toward finding optimal telescope sites. A good telescope environment is uniform in temperature and free from turbulent air. Observatory domes are unheated, and the telescope mirror, which is usually in an open-tube framework, receives special ventilation. In spite of extensive effort and great care to increase resolution, seeing disks in the range of 1 to 2 arc sec are the general rule at most observatories, with rarer periods of sub-arc-sec seeing.

The Earthbound View

A model proposed by F. Roddier describes the seeing conditions in atmospheric turbulence [1]. By considering time intervals of less than 10 ms, the turbulence in the atmosphere can be treated as a frozen pattern of phase variations. Figure 1 shows an appropriate frozen pattern during a brief time interval. The incoming wavefront from a distant object above the atmosphere is separated into constant phase cells of dimension r_0 in the plane of the telescope objective. (If there were

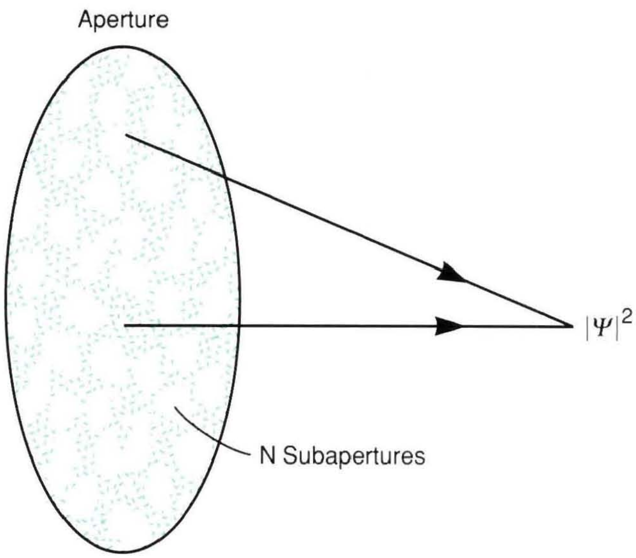

$$|\Psi|^2 = \sum_{i=1}^{N} |\Psi_i|^2 + \sum_{i \neq j} \sum_{j} \Psi_i \Psi_j^*$$

	Seeing Disk	Sum of Uncorrelated Random Phasors
Applicable Spatial Frequencies	Low	High
Intensity ~	N	$N^{1/2}$
Power ~	N^2	N
Normalized Power ~	1	$1/N$

Fig. 1—The division of the telescope aperture into N *effective subapertures. The image results from two independent terms with different dependences on* N. *The first term describes the superposition of the intensities of all the individual subapertures, and the second term describes the interference between the subapertures.*

no atmosphere, the incoming wavefront would have constant phase over the entire objective surface.) In subsequent time intervals, a new cell pattern emerges that is different in detail but similar in statistical properties such as the size and number of the constant-phase cells or effective subapertures. Diffraction theory is used to calculate the resulting image in the telescope focal plane as the sum of the contributions from all the individual subapertures. With a total of N subapertures, each contributing a complex amplitude Ψ_i, the complex amplitude Ψ of the quasi-monochromatic field in the focal plane leads to an illumination, or image intensity, of

$$|\Psi|^2 = \left| \sum_{i=1}^{N} \Psi_i \right|^2 = \sum_{i=1}^{N} |\Psi_i|^2 + \sum_{i \neq j} \sum_{j} \Psi_i \Psi_j . \quad (1)$$

The instantaneous image intensity results from the sum of two different terms in Eq. 1. The first term on the right-hand side of the equation is the incoherent superposition of the intensities of all the individual subapertures. Since the subapertures are assumed to be r_0 in size, the diffraction limit θ_d for a subaperture is given by

$$\theta_d = \frac{0.12}{r_0} .$$

This contribution to the image intensity, which describes the seeing disk, contains no high-spatial-frequency information. Figure 2 shows the relationship between spatial frequencies in the focal plane and distances in the objective planes.

The second term in Eq. 1, a sum of cross products, describes the interference between the subapertures. In effect, the subapertures form a multiaperture interferometer with random phase differences between the separate elements. The second term contains high-spatial-frequency information from all the various orientation and baseline combinations present in the subaperture pairs.

The combination of the two terms in Eq. 1 produces an instantaneous image of the puffed seeing disk, with two primary features. The image fills the seeing disk, described by the first term, within which there is a fine scale structure of bright spots or patches called *speckles*, described by the second term. The speckles contain spatial frequency information up to the diffraction limit of the telescope, but the speckle pattern changes rapidly, generally lasting for time durations less than 10 to 20 ms.

Modern Solutions to Atmospheric Distortion

Attempts to overcome the seeing problem created by atmospheric distortion have taken two approaches. In the first approach, mechanical compensation of a mirror in the light path

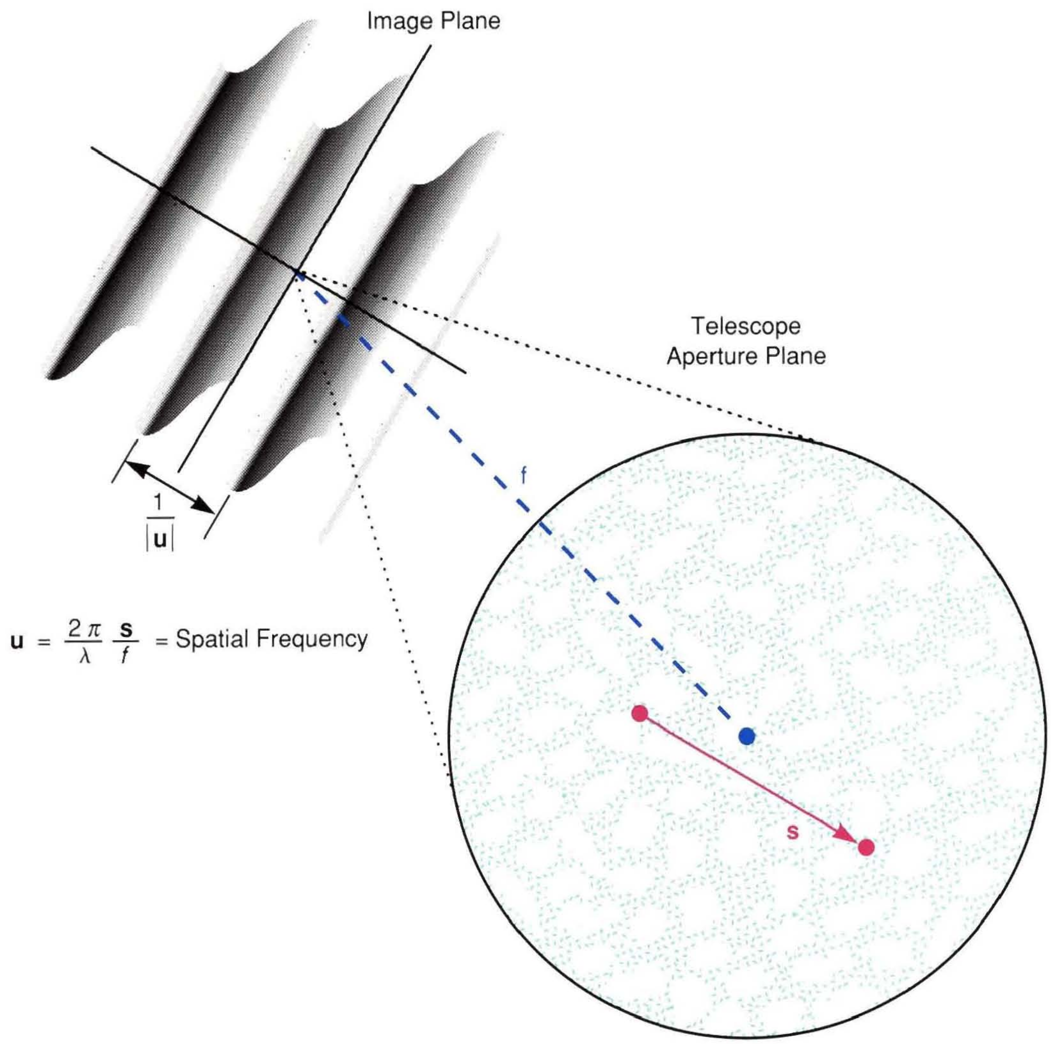

Fig. 2—The relationship between spatial frequencies in the image plane, and separations in the telescope aperture plane.

produces real-time corrections to the wavefront distortions [2]. In the second approach (described in this article), a reconstructed image is obtained by calculating the Fourier transform of the combination of amplitude and phase map produced by the evaluation of the power spectra and bispectra for thousands of noisy short exposures.

Speckle Interferometry

Astronomers in the past two decades developed several techniques to minimize the effects of atmospheric distortion. In 1970 A. Labeyrie made the first major contribution when he noted that the speckle structure in very-short-exposure astronomical images was similar to the structure observed with laser-illuminated diffusers [3]. He applied a formalism to the problem (similar to what follows below) and extracted high-spatial-frequency information not previously available to astronomers. The process he developed is known as *speckle interferometry.*

Let $i(\mathbf{x})$ represent the observed two-dimensional image $i(x, y)$, and let $o(\mathbf{x})$ represent the corresponding object $o(x, y)$. The combined telescope-atmosphere point-spread function $t(\mathbf{x})$ describes the light distribution when a point of light is imaged by the telescope. In this isoplanatic case (see the box, "Isoplanatism"),

$$i(\mathbf{x}) = o(\mathbf{x}) * t(\mathbf{x}) \tag{2}$$

where $*$ denotes the two-dimensional convolution for the imaging process. In the Fourier transform, or spatial-frequency representation, of Eq. 2, the isoplanatic condition is written as

$$I(\mathbf{u}) = O(\mathbf{u}) \bullet T(\mathbf{u}) \tag{3}$$

where $\mathbf{u}$ is the two-dimensional spatial-frequency variable corresponding to the spatial variable $\mathbf{x}$.

Labeyrie faced an experimental dilemma. A highly magnified image of a point source such as a star could be obtained in a brief photographic exposure. However, the high magnification spread the light on his detector so that little total exposure resulted. Clearly, a single exposure that froze the turbulence was not sufficient. Additional exposures could be made, but they produced different samples of the turbulence, and averaging many exposures directly would simply reproduce the bad seeing result. Instead, Labeyrie concentrated his attention on the power spectra of the set of frames. The time average of the power in Eq. 3 is

$$< |I(\mathbf{u})|^2 > = |O(\mathbf{u})|^2 \bullet < |T(\mathbf{u})|^2 > . \tag{4}$$

The left-hand side of Eq. 4 is the time-average power spectrum of the image. It can be determined in any experiment in which a sequence of short exposures is collected. The right-hand side of Eq. 4 contains two terms: the first term, $|O(\mathbf{u})|^2$, is the power spectrum of the object (assumed to be constant during the exposure); the second term, $<|T(\mathbf{u})|^2>$, is the transfer function for the combined telescope-atmosphere system. The second term can, in principle, be evaluated by a separate measurement of a point source (such as a star) under the same seeing conditions. Once the measurement has been done, Eq. 4 can be solved for the object's power spectrum. This technique has been extensively applied to measurements of close double-star pairs [4]. Image reconstruction is not possible with the Labeyrie technique, however, because the object's power spectrum contains information only about amplitudes, and not about the object's phases. With simple objects such as double stars, the power spectrum reveals only the angular separation, orientation (with redundancy of 180°), and magnitude difference between the star pair. With more complicated objects, such as satellites, speckle interferometry is not appropriate, and considerable effort has gone into finding methods to obtain phase information for the optical imaging task [5].

Phase-Recovery Techniques

The Knox-Thompson (KT) method, one of the first studies to provide impressive results on the recovery of object phases, appeared in 1974 [6]. The KT method utilizes a general second-order moment, or cross spectrum, instead of a power spectrum. By substituting expressions like $<I(\mathbf{u})I^*(\mathbf{u} + \Delta\mathbf{u})>$ for the power spectrum, Eq. 4 becomes

$$< I(\mathbf{u})\, I^*(\mathbf{u} + \Delta\mathbf{u}) > = O(\mathbf{u})\, O^*(\mathbf{u} + \Delta\mathbf{u}) \bullet < T(\mathbf{u})\, T^*(\mathbf{u} + \Delta\mathbf{u}) > \tag{5}$$

where only spatial-frequency differences up to a value of half the seeing limit, or $|\Delta\mathbf{u}| \leq 0.5\, r_0/\lambda$, are considered. When telescope aberrations are negligible, the cross-spectral transfer function $<T(\mathbf{u})T^*(\mathbf{u} + \Delta\mathbf{u})>$ is real. Thus the left-hand side of Eq. 5 yields a complex quantity with a phase difference that can be associated with the object. Integration of the phase differences produces a map of the object phases. By combining the phases from the KT method with amplitudes obtained by the Labeyrie procedure, an image is reconstructed. This method has been applied successfully to applications in astronomical imaging [7].

Although the formalism given above describes the calculations in the spatial-frequency domain $I(\mathbf{u})$, a description in the image plane $i(\mathbf{x})$ could be used instead. In the image-plane description, Eqs. 3, 4, and 5 would be correlation calculations implied by the defining convolution. Computational convenience usually determines the description actually employed.

Isoplanatism

The fundamental premise of speckle imaging is that the short-exposure image results from the convolution of the object and the instantaneous atmosphere-telescope point-spread function as expressed in Eq. 2. Implicit in this equation is the assumption that the point-spread function is the same for all parts of the object. If the distortion is identical over the entire image plane, then the distortion is *isoplanatic.*

Isoplanatism is strictly valid only for small viewing angles, since light from widely separated points in the sky will suffer different atmospheric distortions. A simple geometric model yields a first-order approximation for the isoplanatic angle. Assume that all of the distortions occur in a thin layer of the atmosphere at a distance h from the telescope, and that a coherence length r_0 characterizes the wavefront distortion, as shown in Fig. A.

The distortions for two point sources, or different parts of the same object, will be well correlated if their angular separation is less than $\approx r_0/2h$. Under typical good seeing conditions when $r_0 \approx 10$ cm, an atmosphere layer at h = 10 km would produce an isoplanatic angle of approximately 1". If the dominant seeing factor were boundary-layer effects at about 0.5 km, the isoplanatic angle would be 20". Neither of these simple cases represents the real situation, in which many different layers of atmosphere contribute to the distortion. During actual observations, typical values for the isoplanatic angle range from 1 to 4 arc sec [1]. The two-dimensional extension of this concept is the isoplanatic patch. Generally, in good seeing the isoplanatic condition holds for a region of the sky within a patch of $\approx$3" diameter. The danger that nonisoplanatism presents is not that it destroys the signal, but that it produces distortions that present difficulties to the processing and reconstruction procedures.

References

1. F. Roddier, J.M. Gilli, and J. Verin, "On the Isoplanatic Patch Size in Stellar Speckle Interferometry," *J. Optics (Paris)* **13**, 63 (1982).

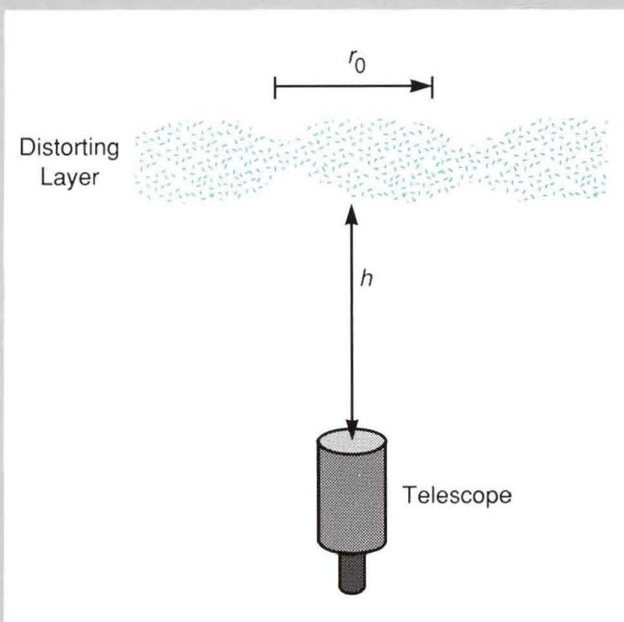

Fig. A. A simple geometric model leads to an approximation for the isoplanatic angle.

The Bispectrum

Between 1977 and 1983 several astronomers in the Federal Republic of Germany developed an improvement to the Labeyrie and KT approach [8]. Originally called *speckle masking*, the improved technique is now known as *bispectrum* or *triple correlation*. In this procedure each of the quantities of interest is defined as a triple correlation in the image plane; its Fourier transform is a bispectrum. For example, instead of the image intensity $i(\mathbf{x})$, the triple correlation is

$$b(\mathbf{x}_1, \mathbf{x}_2) = \int i(\mathbf{x}) \cdot i(\mathbf{x} + \mathbf{x}_1) \cdot i(\mathbf{x} + \mathbf{x}_2)\, d\mathbf{x} .$$

The corresponding Fourier-transform bispectrum is

$$\begin{aligned} B_I &= B(\mathbf{u}_1, \mathbf{u}_2) \\ &= I(\mathbf{u}_1) \cdot I(\mathbf{u}_2) \cdot I^*(\mathbf{u}_1 + \mathbf{u}_2) . \end{aligned} \tag{6}$$

Similar definitions are appropriate for the object and the telescope point-spread functions. Combining Eq. 3 with the definitions above produces the relationship

$$B_I = B_O \cdot B_T . \tag{7}$$

The apparent simplicity of Eq. 7 belies the computational effort needed in any real application. The bispectrum is a complex-valued function of two spatial-frequency vectors, or, equivalently, four real variables. In an application in which averages over all the frames are needed, the equation becomes

$$< B_I > = B_O \cdot < B_T > . \tag{8}$$

The bispectrum can be considered a generalization of the phase-closure technique employed in radio astronomy [9]. The bispectrum is composed of products of terms for three spatial frequencies that form a closed vector triangle, as shown in Fig. 3. As a result of the vector closure, the closure phase for the $<B_T>$ term in Eq. 8 is zero. The complex value of the calculated bispectrum $<B_I>$ thus yields a phase term that may be identified as the phase of the object's bispectrum B_O in Eq. 8. The choice of spatial frequencies in the bispectrum definition leads to the cancellation of the atmospheric phase distortions. Many short exposures are necessary to provide the B_I values from which the average is determined.

The process can be visualized by the following relationships. Since a simple proportionality exists between spatial frequency **u** and **s** (the corresponding linear separation in the aperture plane—see Fig. 2), each vector triple product in Eq. 6 can be associated with a set of triangles (all the same size and orientation) in the telescope aperture. Figure 4 shows a sample subset of the triangles for this example. For short time intervals, the atmospheric distortions form a frozen pattern of effective subapertures, as shown in the speckled background within the aperture. Each triangle represents a sampling of the aperture plane by a three-element interferometer with three baselines. The phase of the speckle transfer function B_T is written as

$$\begin{aligned} \text{Phase}\,[B_T] &= \text{Phase}\,[T(\mathbf{u}_1) \cdot T(\mathbf{u}_2) \cdot T(-\mathbf{u}_1 - \mathbf{u}_2)] \\ &= \text{Phase}\left[\sum_{j=1}^{n} \sum_{k=1}^{n} \sum_{l=1}^{n} \exp\,(i\,\theta_{jkl})\right] \end{aligned}$$

$$\text{where} \quad \theta_{jkl} = \theta_j^{\mathbf{u}_1} + \theta_k^{\mathbf{u}_2} + \theta_l^{-\mathbf{u}_1 - \mathbf{u}_2} .$$

The terms in the sum with $j = k = l$ cancel because of phase closure. There are n such terms and they define the desired signal in the sum. In $3n(n-1)$ terms two of the indices are equal. Only partial cancellation occurs for these terms, which contributes some noise to the process. Similarly, there are $n(n-1)(n-2)$ terms with

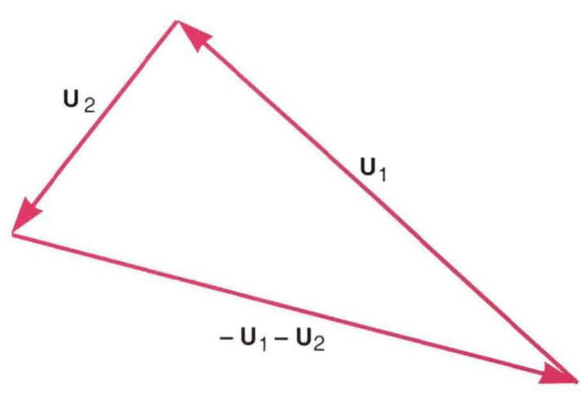

Fig. 3—The bispectrum spatial-frequency triangle.

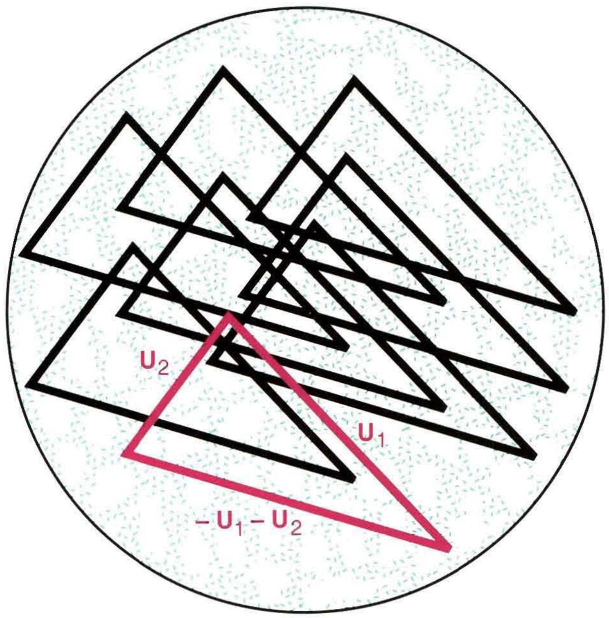

Fig. 4—Sample subset of aperture-plane phase-closure baseline triangles for a given pair of $\mathbf{u}_1$ *and* $\mathbf{u}_2$ *values.*

$j \neq k \neq l$. These terms represent the dominant source of noise. With a random-walk model for this portion of the triple product, the length of the resultant noise phasor can be estimated as $n^{3/2}$. If M frames are chosen to average out the statistics of the atmosphere, the length of the resultant noise phasor is on the order of $M^{1/2} \cdot n^{3/2}$, and the desired signal vector is of length $M \cdot n$. For the desired signal to outweigh the noise, M frames must be averaged so that $M \cdot n >> M^{1/2} \cdot n^{3/2}$, or $M >> n$. Under these conditions the phase of the speckle transfer function approaches zero.

The ideas in the previous paragraph suggest a strategy for simplifying the computations. If all the triple products are chosen so the reference vector $\mathbf{u}_1$ is arbitrary and the offset vector $\mathbf{u}_2$ is small, then the noise phasors are not completely random, and more phase cancellation can occur. This recognition suggests the implementation of a selected subset of the full bispectrum, which reduces computational effort with little information loss. For the bispectra calculations described in this article, the offset vector was limited to values of six pixels or fewer in length. Although the length restriction on the offset vectors significantly reduces the computational task, each frame still requires over 60,000 triple-product evaluations.

It is instructive to examine how the bispectrum B_O preserves object-phase information. Figure 4 shows examples of the bispectrum spatial-frequency triangles that correspond to three-element interferometers in the aperture plane, for a single pair of $\mathbf{u}_1$ and $\mathbf{u}_2$ values. The atmosphere phase delay at a given vertex contributes to two baselines and, in the sum of phase delays around the entire triangle, these phase delays cancel out. This is the essence of phase closure. For the object, however, the phase difference for a given arm of the triangle interferometer will be the same wherever that arm is in the aperture, provided that the size and orientation of the triangle do not change. Similar reasoning applies to the second and third arm of the triangle, and for all triangles at all spatial frequencies. The phase difference produced by the object between the light sampled at subapertures at the left and upper vertex of each of the triangles in Fig. 4 should be identical. The phase differences produced by the object do not depend on position in the aperture, provided that the light samples have the same separation and relative orientation. In contrast, the strong positional dependence of the atmospheric phase pattern is exactly what causes cancellation in the bispectrum processing.

Once the bispectrum B_O has been calculated, a recursion relation is employed to reconstruct the actual phase map of the object's Fourier transform. With the phases Φ for the initial spatial-frequency values $\mathbf{u}_1$ and $\mathbf{u}_2$, the phase $\beta(\mathbf{u}_1, \mathbf{u}_2)$ of the bispectrum $B(\mathbf{u}_1, \mathbf{u}_2)$ is used to calculate object phase $\Phi(-\mathbf{u}_1 - \mathbf{u}_2)$:

$$\Phi(-\mathbf{u}_1 - \mathbf{u}_2) = \beta(\mathbf{u}_1, \mathbf{u}_2) - \Phi(\mathbf{u}_1) - \Phi(\mathbf{u}_2) . \qquad (9)$$

The calculation assumes the initial conditions $\Phi(\mathbf{0}) = \Phi(\mathbf{1}) = 0$, and then proceeds to higher frequencies. The above assumptions influence only the position of the object in the frame, not the structure of the image.

Figure 5 outlines the computational procedure that implements the bispectrum calculation. The data set, which consists of a sequence of time-tagged photon addresses, is divided into individual frames. The Fourier transform of each frame is calculated and input to both the upper and lower tracks in the computational flow. The upper track in Fig. 5 represents the calculation of the power spectrum for the image. The power, computed for all the image frames of the observed object, is divided by the power of the corresponding point-spread function of the atmosphere-telescope combination in the stellar-interferometer approach described earlier. The lower track of Fig. 5 indicates the computation of the bispectrum for the image by obtaining the object's phase map according to Eq. 9. The power spectrum of the image produces the spatial-frequency amplitudes, the bispectrum produces the necessary phases, and the image is reconstructed by calculating the inverse Fourier transform. A practical feature of the implemented calculation is the insertion, near the end of the upper track in Fig. 5, of a low-pass filter for the power spectrum. The filter sets an upper limit to the highest spatial frequency used in the reconstruction, and serves to reduce the impact of noise in the reconstruction process.

Photon-Noise Bias in Computed Bispectra

Photon noise is an important source of degradation in reconstructing images from low-light-level measurements. In recent years the use of the bispectrum to reconstruct images has become popular, and the contribution of photon noise to this computation has been analyzed. In general these analyses assume that the imaging detector has a uniform sensitivity across its aperture. In practice, detectors are not uniform, however, and their nonuniformity has an impact on the computation of the photon-noise bias.

Photon-noise bias removal is an important step in reconstructing images observed through the atmosphere. Short-term exposures, called frames, are taken by a photon-counting camera and used to estimate the image bispectrum from which the image is reconstructed. If the object being imaged is very dim, or the exposure time for a single frame is very short, the computed bispectrum will contain a photon-noise component resulting from the Poisson statistical nature of the photon-detection process. The accurate reconstruction of an image under these low-light-level conditions requires that the biases introduced by the photon noise be removed.

The contribution of the photon noise to the computed power spectrum was derived by J. W. Goodman and J.F. Belsher in 1976 [10]. This result was extended to the bispectrum computation by B. Wirnitzer in 1985 [11]. Both of these results assumed that the detection process was uniform over the field of view. However, practical photon-counting cameras, such as the Preci-

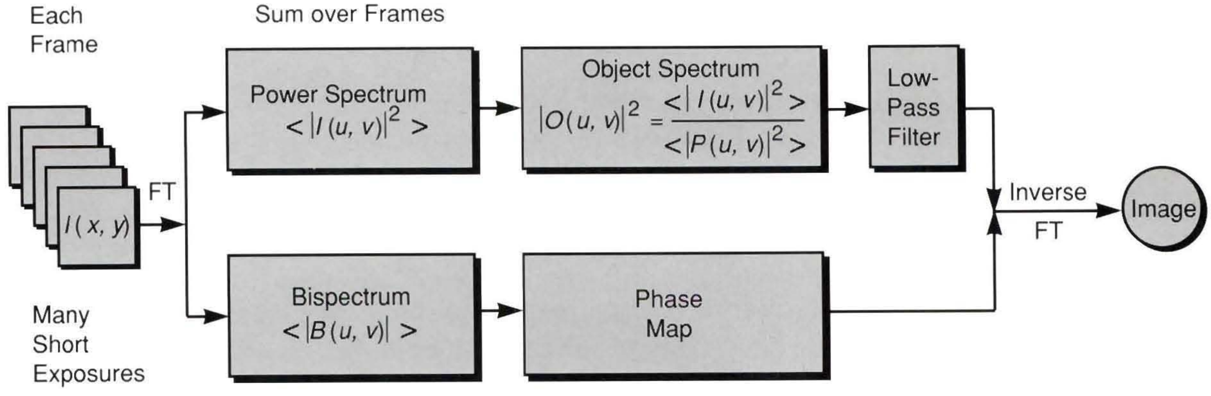

Fig. 5—The computational process for speckle-image reconstruction. A single image results from a set of many individual short exposures.

sion Analog Photon Address camera (PAPA) [12], are not uniform. Because of engineering tolerances and differing detector sensitivities, some pixels will be brighter than others when the camera is exposed to uniform illumination. S. Ebstein addressed the problem of photon-noise bias for a nonuniform camera in the computation of the power spectrum estimate [13]. Here we derive the photon-noise component of the bispectrum estimate for a nonuniform camera.

We want to recover an image $i\,(\mathbf{x})$ by estimating various quantities from the list of detections. Note that $i\,(\mathbf{x})$ will contain the effects of atmospheric distortion (recall Eq. 2), but the photon-noise bias and the effects of a nonuniform camera will have been removed. In particular we are interested in estimating the image bispectrum B_I. To begin we create a frame of N photon detections from the list of detections by using the appropriate pixel weights obtained from calibrating the camera with a uniform illumination. The frame is given by

$$d(\mathbf{p}) = a(\mathbf{p}) \sum_{n=1}^{N} \delta(\mathbf{p} - \mathbf{p}_n) .$$

The variable $\mathbf{p}$, which may be interpreted as a two-dimensional spatial variable, is the pixel index. Similarly, $\mathbf{p}_n$ is the pixel location of the nth detected photon. By taking the Fourier transform of $d(\mathbf{p})$ we obtain

$$D(\mathbf{u}_1) = \sum_{\mathbf{p}} d(\mathbf{p})\ e^{-i2\pi\mathbf{u}_1 \cdot \mathbf{p}}$$

$$= \sum_{n=1}^{N} a(\mathbf{p}_n) \exp\left[-i2\pi\mathbf{u}_1 \bullet \mathbf{p}_n\right] .$$

The variable $\mathbf{u}_1$ is a two-dimensional spatial-frequency variable; it might be best to think of it as a vector, for example, $\mathbf{u}_1 = (\, u_x, u_y\,)$.

The bispectrum of $i\,(\mathbf{p})$ is given by

$$B_I(\mathbf{u}_1, \mathbf{u}_2) = I(\mathbf{u}_1) \bullet I(\mathbf{u}_2) \bullet I(-\mathbf{u}_1 - \mathbf{u}_2) .$$

Note that the bispectrum is a complex function of four variables, since $\mathbf{u}_1$ and $\mathbf{u}_2$ both represent two-dimensional spatial-frequency variables. The bispectrum is useful for image reconstruction because, unlike the power spectrum, the bispectrum retains phase information [14].

We want to estimate $B_I(\mathbf{u}_1, \mathbf{u}_2)$ from the list of detections that our camera has recorded. We can compute $D(\mathbf{u}_1)$ from the list of detections $d(\mathbf{p})$ for a particular frame, and then form the bispectrum

$$B_D(\mathbf{u}_1, \mathbf{u}_2) = D(\mathbf{u}_1) \bullet D(\mathbf{u}_2) \bullet D(-\mathbf{u}_1 - \mathbf{u}_2) .$$

By using the definition of $D(\mathbf{u}_1)$ we get the triple product

$$B_D(\mathbf{u}_1, \mathbf{u}_2) = \sum_{j=1}^{N} \sum_{k=1}^{N} \sum_{l=1}^{N}$$

$$a(\mathbf{p}_j)\, a(\mathbf{p}_k)\, a(\mathbf{p}_l)\ e^{-i2\pi[\mathbf{u}_1 \cdot (\mathbf{p}_k - \mathbf{p}_l) + \mathbf{u}_2 \cdot (\mathbf{p}_j - \mathbf{p}_l)]} .$$

Now we take the expected value over the detection process following the derivation of Wirnitzer [11]. In practice this is estimated by averaging over a suitably large number of frames:

$$\varepsilon[B_D(\mathbf{u}_1, \mathbf{u}_2)] = N\varepsilon[a^3(\mathbf{p})]$$

$$+ \frac{N(N-1)}{I^2(0)} \left[I_2(-\mathbf{u}_1)\, I(\mathbf{u}_1) + I_2(-\mathbf{u}_2)\, I(\mathbf{u}_2) + I_2(\mathbf{u}_1 + \mathbf{u}_2)\, I(-\mathbf{u}_1 - \mathbf{u}_2)\right]$$

$$+ \frac{N(N-1)(N-2)}{I^3(0)}\ B_I(\mathbf{u}_1, \mathbf{u}_2) . \qquad (10)$$

The constant $I(0)$ is simply the sum of the image values $i\,(\mathbf{p})$ over all pixels $\mathbf{p}$. Thus $I^2(0)$ is the total power in the image. The spectrum I_2 is the Fourier transform of weighted image $a\,(\mathbf{p})i\,(\mathbf{p})$. The term $\varepsilon[a^3(\mathbf{p})]$ is the average of the cubed weights over all detections in all frames.

The last term in Eq. 10 is the term of interest, and for bright objects the last term dominates. The first two terms comprise the photon-noise bias that must be eliminated. Note that the second term is frequency dependent and is complex in general. It will tend to corrupt both the phase and the magnitude of the bispectrum estimate.

Wirnitzer suggested the use of an estimator $Q(\mathbf{u}_1, \mathbf{u}_2)$ for the bispectrum, which is given by

$$Q(\mathbf{u}_1, \mathbf{u}_2) = B_D(\mathbf{u}_1, \mathbf{u}_2) - |D(\mathbf{u}_1)|^2 - |D(\mathbf{u}_2)|^2 - |D(-\mathbf{u}_1 - \mathbf{u}_2)|^2 + 2N .$$

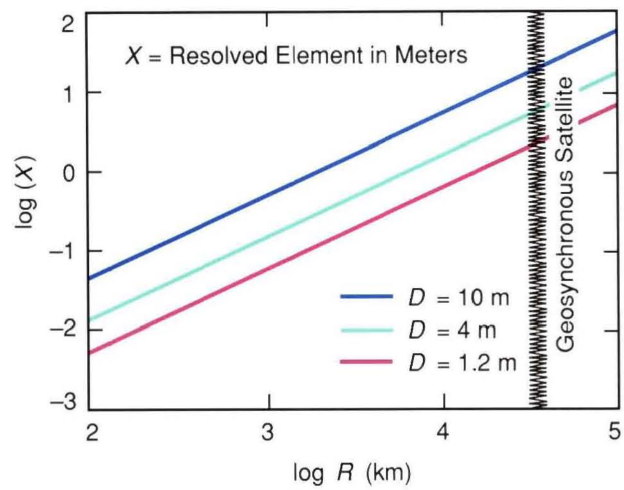

Fig. 6—For diffraction-limited resolution, the smallest resolvable element X is proportional to the line-of-sight distance R to the object, and inversely proportional to the telescope aperture diameter D. Submeter optical resolution for telescopes less than 10 m in diameter is possible only for objects at distances less than 2,000 km.

For the case of a uniform linear detector, Wirnitzer showed that the expected value of Q is proportional to the desired B_I. From the above results it is straightforward to show that if the detector is nonuniform, then Q is not unbiased. However, we can generalize $Q(\mathbf{u}_1, \mathbf{u}_2)$ to be

$$Q(\mathbf{u}_1, \mathbf{u}_2) = B_D(\mathbf{u}_1, \mathbf{u}_2) - D(\mathbf{u}_1)\, S(-\mathbf{u}_1) - D(\mathbf{u}_2)\, S(-\mathbf{u}_2) - D(-\mathbf{u}_1 - \mathbf{u}_2)\, S(\mathbf{u}_1 + \mathbf{u}_2) + 2 \sum_{n=1}^{N} a^3(\mathbf{p}_n)$$

where $S(\mathbf{u}_1)$ is the Fourier transform of the weighted image $a(\mathbf{p})d(\mathbf{p}) = a^2(\mathbf{p})\delta(\mathbf{p} - \mathbf{p}_n)$. Then when Q is averaged over all the frames, it will be proportional to the desired bispectrum B_I:

$$\mathcal{E}[Q(\mathbf{u}_1, \mathbf{u}_2)] = \frac{N(N-1)(N-2)}{I^3(0)}\, B_I(\mathbf{u}_1, \mathbf{u}_2)\,.$$

The Satellite Problem

The application of speckle-imaging techniques to satellite imaging differs in three primary respects from astronomical applications. These three differences or limitations define the domain of application.

The first limitation is the size of the smallest resolved satellite feature. If the telescope diffraction limit is the desired performance goal, the size of the smallest resolvable satellite feature will be proportional to the actual distance to the observed satellite. Since typical satellite dimensions range from 2 to 20 m, a realistic imaging goal would be to achieve resolutions of 10 to 20 cm. Figure 6 shows that the application of speckle imaging is limited to near-earth satellites, particularly satellites within 2,000 km of the observing site.

The second limitation is the length of time during which photons may be collected for a single exposure frame. In astronomical applications the collection time is determined by how quickly the atmosphere above the telescope changes across the optical path. In astronomical speckle observations, frame-time intervals of 10 to 20 ms are appropriate, and isoplanatic conditions prevail. For satellites near the earth, the rapid motion (up to several thousand seconds of arc per second) across the line of sight effectively moves them out of one isoplanatic region into another in a few milliseconds. As a consequence, the frame time for satellite observations must be less than the frame time for astronomical observations.

The third limitation occurs because the satellite undergoes motions that include rapid rotation, changes in orientation and aspect, and changes in apparent size due to the rapidly changing distance of the satellite from the observer. As a result, the total time available to collect frames for a given image reconstruction is limited. With rapidly rotating satellites the time limit is on the order of fractions of a second. Fortunately, the motion is much slower for many of the objects of greatest interest. The limiting factor often is a change in the satellite aspect to the observer during the pass, or a substantive change in solar illumination resulting from changes in the geometry of the sun-satellite-observer configuration. The exposure time limit set by these factors is generally on the order of 3 to 10 s for objects within 2,000 km. Again, this time limitation is not a consideration in the astronomical application of the technique

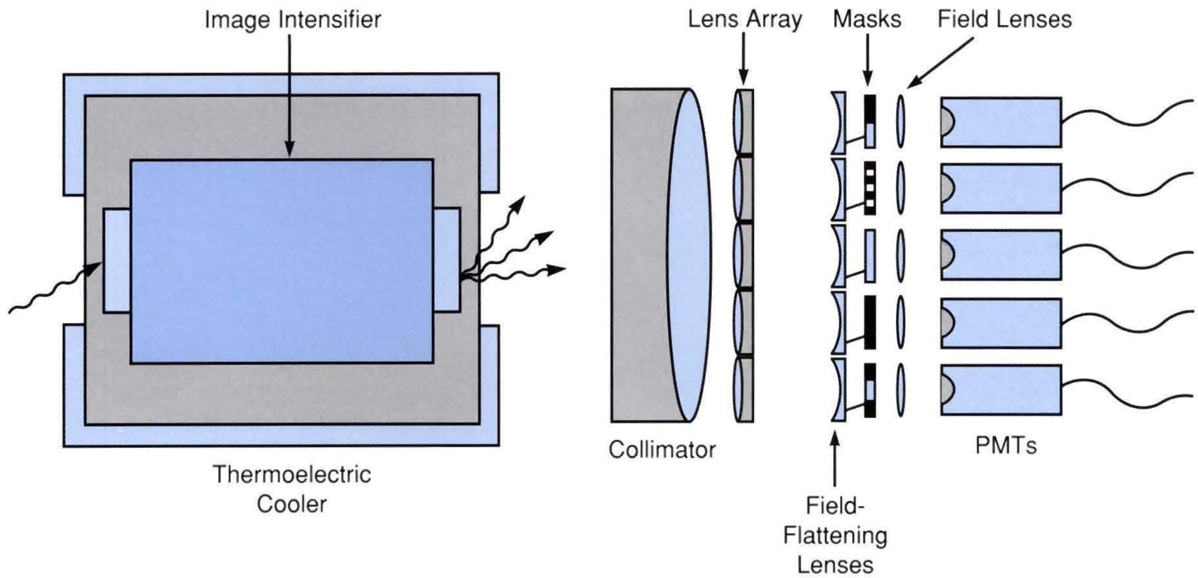

Fig. 7—Schematic diagram of the Precision Analog Photon Address (PAPA) two-dimensional photon detector.

in which total exposures of minutes or hours are possible.

Detectors

The success of speckle-imaging experiments has followed the development of detectors with necessary features for recording the images. For the detection of satellite images, as many photons as possible are required in frame times of a few milliseconds for a total period of a few seconds. A fast rate of detection calls for a sensitive two-dimensional detector with a fast response. Furthermore, the two-dimensional response needs to be a faithful representation of the incident light level, and the detector should introduce as little additional noise as possible.

The detector chosen for these experiments was the Harvard Precision Analog Photon Address (PAPA) camera [12]. Figure 7 shows a schematic diagram of the PAPA detector. The highly magnified speckled image is focused on the face of the high-gain image intensifier at the front of the camera. Each photon detected at the photocathode face produces a bright spot at the output of the intensifier. In this way the intensifier converts the relatively faint image to a brighter image made up of bright spots at the tube output phosphor. The PAPA detector's second stage, a combination of lenses and masks, records the position and time of arrival of each bright spot. A large single lens collimates the light from the output phosphor. In this collimated beam 18 pairs of smaller lenses reimage the phosphor onto 18 different masks, nine for the x-coordinate and nine for the y-coordinate of each bright spot. The mask sets are half-open and half-closed Grey-code spatial filters; each mask is divided into divisions finer by factors of two than the previous mask in the set. The light passed by the masks reimages onto one of 18 small photomultiplier tubes. Fast gate integrators integrate the outputs of the photomultiplier tubes. A separate strobe photomultiplier, which has no mask, signals that a bright spot is produced somewhere on the phosphor face. The location of the spot is then recorded by latching the output of the 18 photomultipliers and resetting the integrators for the next bright spot (i.e., photon detection). The image data is thus a stream of time-tagged photon addresses that are encoded on a video carrier and recorded serially on a video tape.

The PAPA camera converts each detected photon into a time and an address. The noise associated with the detection process is due only to photon noise, an inherent limiting noise in any photon process. For the PAPA camera, photon noise is significant only when the number of recorded photons per frame is small, which occurs in satellite speckle imaging. Other detectors overcome photon noise less effectively. A CCD image frame has additional readout noise, while detectors with stages of multiplication or scanning introduce other noise terms such that photon noise is not the limiting factor. As described earlier in the section "Photon-Noise Bias in Computed Bispectra," the evaluation of the photon noise in each PAPA frame, when we take into account the nonuniform sensitivity across the detector face, is crucial to the success of the image reconstruction process.

Laboratory Experiments

Three primary sources of data are used to demonstrate and test the speckle-image-processing algorithms and procedures described in this article: computer simulation of an object, imaging system, detector, and seeing conditions; a laboratory setup with artificially produced poor seeing; and actual telescope observation of an object through the atmosphere. The results reported here are limited to laboratory setups and actual telescope observations. In particular, laboratory experiments, in which control over specific experimental parameters is possible, are especially valuable in gaining an understanding of the trade-offs involved.

Figure 8 shows a diagram of the laboratory setup. Several methods exist for producing laboratory seeing conditions similar to those encountered at the telescope. These methods include heating the air in the optical path, circulating a medium such as water or oil with beads of a different index of refraction, moving a glass surface coated with oil drops or layers of different thicknesses in the light path, and moving an irregular phase plate or glass surface in the beam. We chose the last method for convenience and for the high degree of reproducibility in the data collection. The selected phase screen (a piece of shower glass) rotates in the beam at a rate that provides isoplanatic conditions for up to 0.2 s. Data collection in this experimental arrangement produces longer frame times than those at the telescope. The longer frame times allow subsequent direct comparisons between high-light-level and low-light-level situations.

The laboratory light source was placed behind a diffusing glass. The object for the experiments was a 35-mm slide that combines opaque openings in thin-metal stock overlays with

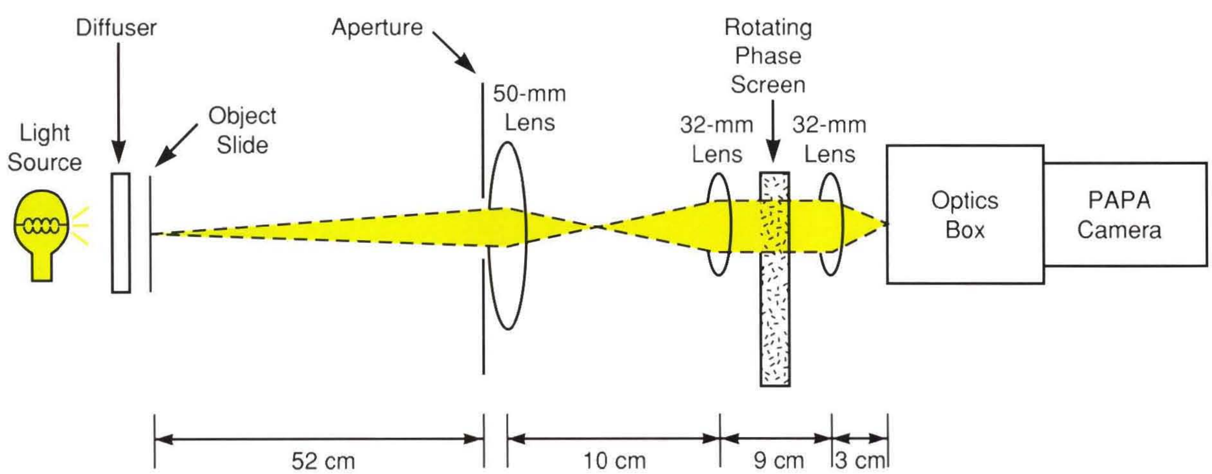

Fig. 8—Schematic diagram of the laboratory setup for producing speckle data to test the image-reconstruction software.

(a) (b)

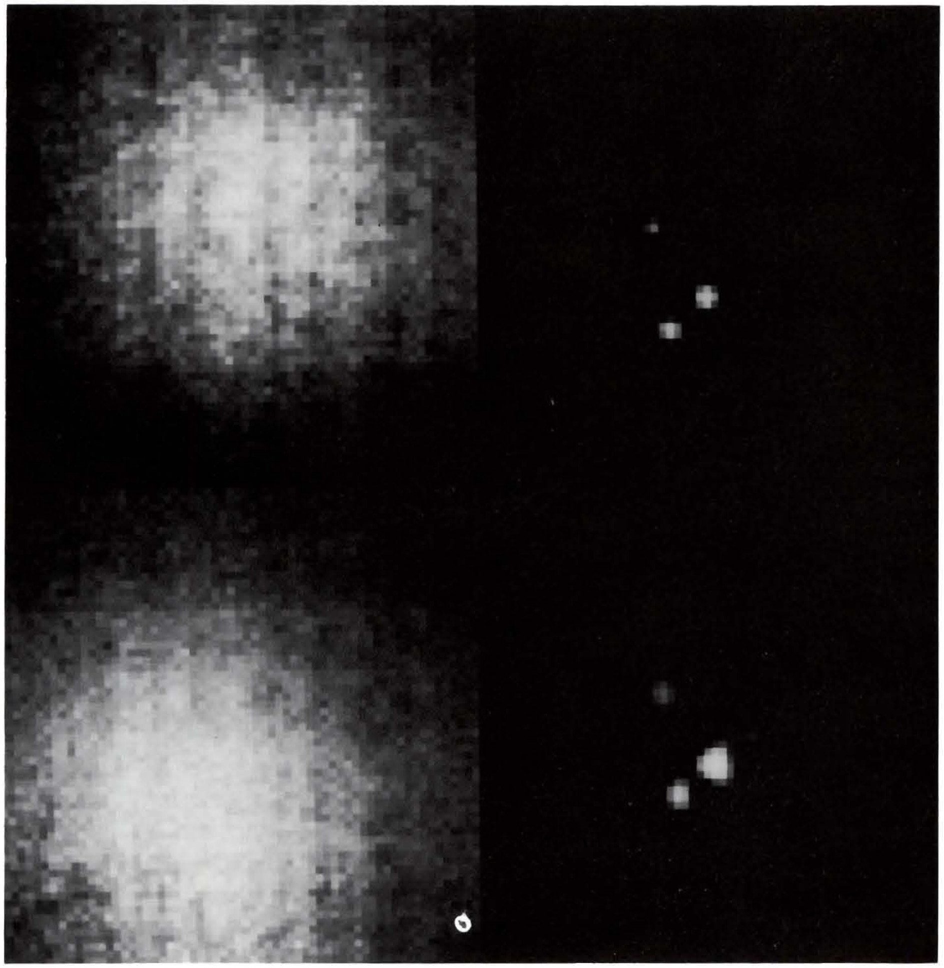

(c) (d)

Fig. 9—Example of speckle-image reconstruction in the laboratory. (a) The seeing-degraded time exposure of a point source. (b) The triple-star test object without seeing degradation. (c) The seeing-degraded time exposure of the triple star. (d) The reconstructed image of the triple-star. Only (a) and (c) are used as input for the calculation.

neutral-density filters to provide the desired shape and brightness variations. In each experiment, an object image was also obtained without a distorting phase plate. The undistorted image provided a reference model from which reference power spectra and bispectra could be obtained.

The following two examples demonstrate the speckle-imaging technique and the image-reconstruction process (see Fig. 5) for two artificial star systems.

Power Spectra Bias Correction

The object is an artificial triple star with three openings of different sizes and brightnesses on a target slide in the laboratory setup (Fig.9[b]). During the experiment a separate measurement for the time exposure of a single unresolved opening or artificial single star (Fig.9[a]) had the same appearance as the typical seeing disk in an astronomical observation. Such a measurement provides the reference measurement needed to evaluate the system speckle transfer function. Although Fig.9(c) is the seeing-degraded triple-star system, it is similar to but larger than the single-star result. The integrated bispectrum for the seeing-degraded triple-star observation yields the phases needed in combination with the derived power spectrum to produce Fig. 9(d), the image reconstruction of the triple-star object, which is a slightly broadened version of the original object (Fig. 9[b]).

An examination of the power spectra for this example dramatically demonstrates the need for proper photon-noise bias treatment. Figure 10(a) displays the power spectrum corresponding to the triple star with no seeing (shown in Fig.9[b]). Notice that the power spectrum contains the expected strong fringe pattern characteristic of a triple-star object. Figure 10(b) shows the power spectrum for a point source with seeing present. The exposure data from the triple star with seeing (Fig.9[c]) is collected. Then the power spectrum, with noise bias removed, is calculated and divided by the bias-corrected power spectrum of the point source with seeing (Fig. 9[a]). Figure 10(c) shows the result of this division; the result produces the estimate of the

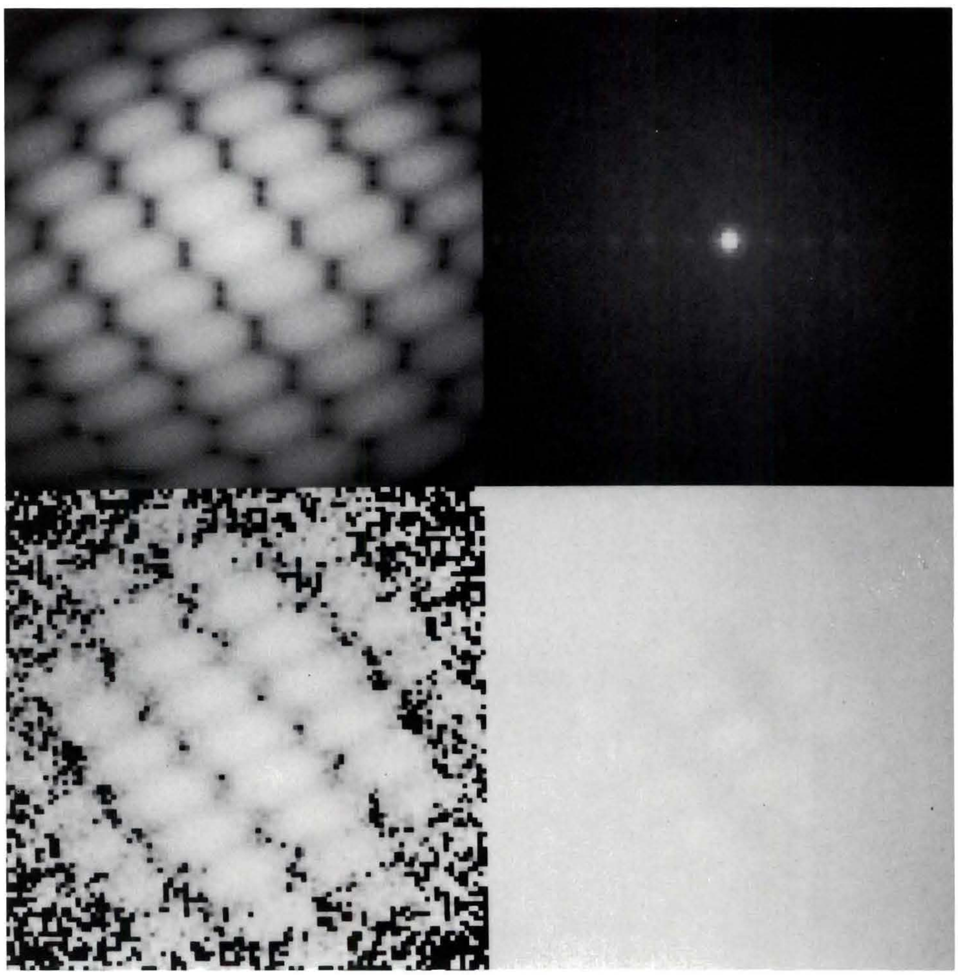

Fig. 10—Demonstration of speckle interferometry for the triple-star test object. (a) The power spectrum in the image of the triple star when no seeing is present. (b) The corresponding power spectrum of a point source with seeing. (c) The power spectrum of the triple star system $|O(\mathbf{u})|^2$ obtained by using Eq. 4 with the data from Fig. 9(a) for $<|T(\mathbf{u})|^2>$ and from Fig. 9(c) for $<|I(\mathbf{u})|^2>$. Proper bias treatment produces a power spectrum that represents the desired result shown in (a). (d) The power spectrum produced with no bias removal in any of the power spectra evaluation. Clearly (d) is not a satisfactory representation of the power spectrum in the image-reconstruction process.

(a) (b)

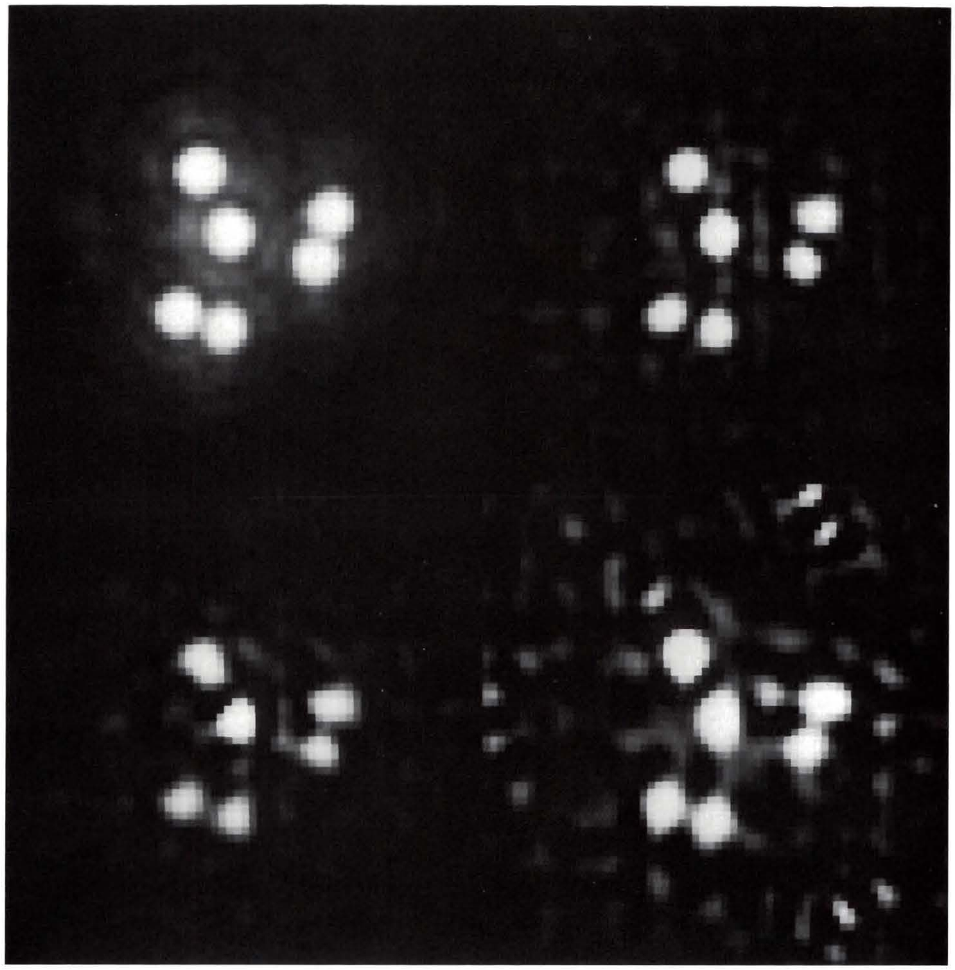

(c) (d)

Fig. 11—A demonstration of the role of proper bias correction. Figures (b), (c), and (d) are image reconstructions with proper bias treatment in the power spectra, but different bias corrections in the bispectra calculations. (a) A six-star object under high-light-level conditions. (b) Proper bias correction. (c) No bias correction. (d) Wirnitzer's [13] bias correction.

power spectrum of the object. Figure 10(d) is the same calculated quantity without bias removal. Figures 10(c) and 10(d) vividly demonstrate the importance of bias treatment of the power spectrum, for Fig. 10(c) is clearly a better representation of Fig. 10(a) than is Fig. 10(d).

Bispectra Bias Correction

The role of the bias treatment in the phase calculation is more subtle, and more difficult to demonstrate. The phase map of the triple-star object is not sufficiently complex for this demonstration. Instead, for high light levels, Fig. 11(a) shows a more complicated six-star system. To prevent bias problems in the power spectra from complicating this example, only properly bias-corrected power spectra are used. Figure 11(b) is a reconstruction of the object; the reconstruction uses the proper bias calculation in the bispectrum. The reconstruction of the object in Fig. 11(c) employs no bispectrum bias correction, while Fig. 11(d) shows the result of applying the bias correction of B. Wirnitzer [11]. All of these images were obtained with high illumination levels. In contrast, Fig. 12 shows the results

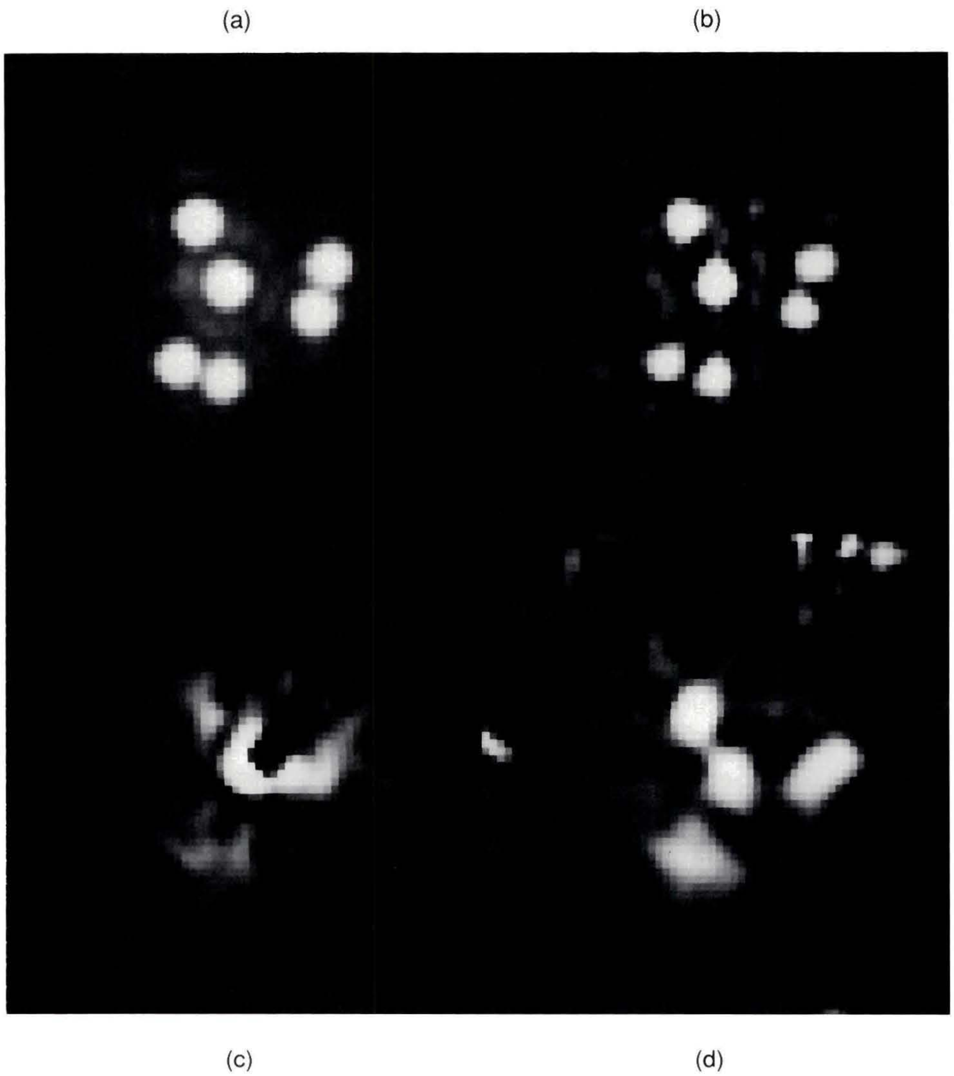

Fig. 12—Same as Fig. 11 except for low-light-level situation. The importance of the proper bias treatment in (b) is obvious.

for identical calculations under low-light-level conditions. The example of Fig. 12 demonstrates that, while the bias calculation is insignificant in high light levels, only proper bias treatment yields images of quality in low light levels. With correct bias treatment, the images in Figs. 11 and 12 are similar. This recognition implies that any other noise introduced to the processing of the low-light-level result produces only minor consequences in these image reconstructions.

Telescope Experiments

The laboratory experiments were useful in developing and testing the image-reconstruction software. Telescope observations, however, are the true test of the reconstruction procedure. The examples below demonstrate the application of speckle-image reconstruction procedures to telescope observations.

Planetary Observations

Figure 13 shows the speckle imaging of Pluto and its satellite Charon. The speckle data were recorded with the Harvard PAPA camera at the 2.5-m Las Campanas observatory telescope in Chile in June 1988. Charon was originally discovered in 1978 by J.H. Christy and R.S.

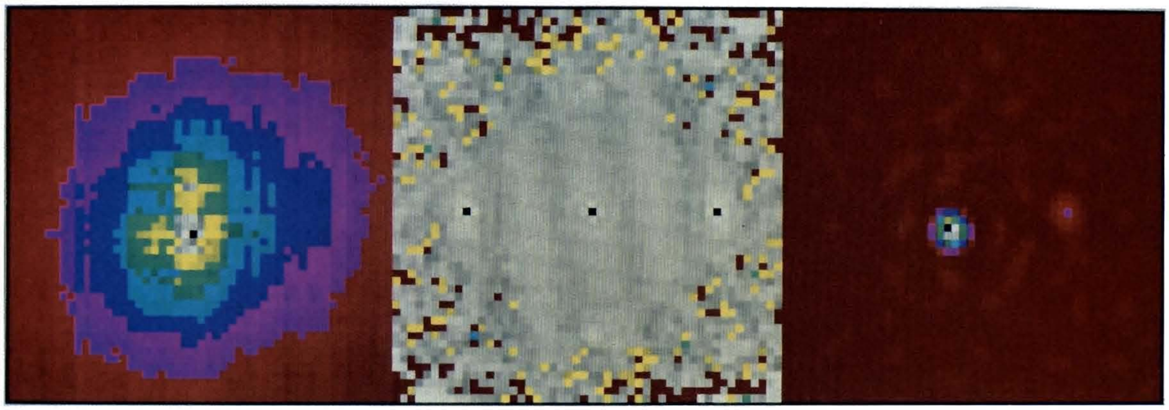

Fig. 13—Image reconstruction of Pluto and its moon, Charon. (a) The long-exposure image of the Pluto-Charon system. (b) The power spectrum of the image. (c) The speckle-image reconstruction of the resolved pair.

Harrington on long exposures with photographic plates [15]. Astronomers have since detected Charon near its maximum elongation position on a number of prediscovery plates. Pluto and Charon are very faint; their combined brightness is 14.9 magnitude. Charon's magnitude is 16.8, about 1/21,000 times as bright as the faintest stars visible to the naked eye. Detection of Charon is difficult because it is usually in such angular proximity to Pluto that it is lost in the glare of the planet's seeing disk, which is five times brighter than Charon. The present precise orbit of the satellite was obtained from a collection of speckle-interferometry observations of the pair gathered in 1984 and 1985 [16]. Figure 13(a) is a long-exposure view of the Pluto system, Fig. 13(b) is the bias-corrected power spectrum of the system, and Fig. 13(c) shows the speckle reconstruction of the same frames. The image in Fig. 13(c) resulted from processing 18,000 separate frames, each with about 30 detected photons. Proper bias correction is crucial at such a low light level.

Star Observations (Seeing Effects)

Experiments conducted at the 1.2-m Firepond telescope in Westford, Mass., during the period 24–29 January 1988, provided a wealth of telescope speckle data. Several cases shown in Figs. 14, 15, and 16 exemplify specific aspects of the speckle-imaging problem.

The following side-by-side comparison demonstrates the success of image reconstruction under different seeing circumstances. Two stars, nearly equal in brightness, were observed on separate evenings. Star 1 (FK436, visual magnitude = 4.5) was observed on a night of average seeing, when the seeing disk was 2 arc sec. Star 2 (FK493, visual magnitude = 4.7) was observed on a night of very good seeing when the seeing disk was 1 arc sec. A reference model was generated for comparison. Since the stars are unresolved beyond point images, they can be represented by mathematical points or delta functions. The image reconstruction is not expected to achieve such precise performance, however, since the telescope aperture and the spatial filter set upper limits to the highest spatial frequencies passed.

In this particular experiment the spatial filter determined the performance limit. The bottom row of Fig. 14 shows the broadening effect of the filters. Shown are spatial-filter-broadened point-source images for filter values 0.2, 0.3, 0.4, and 0.5, respectively. The upper row contains the actual star 1 time exposure followed by speckle-image reconstructions for filter values of 0.2, 0.3, 0.4, and 0.5 as before, and the middle row contains identical measurements for star 2. Even though the seeing was twice as good for star 2, the reconstructed images of the two stars are virtually equal in quality at any corresponding filter value. The spatial filter, not the atmo-

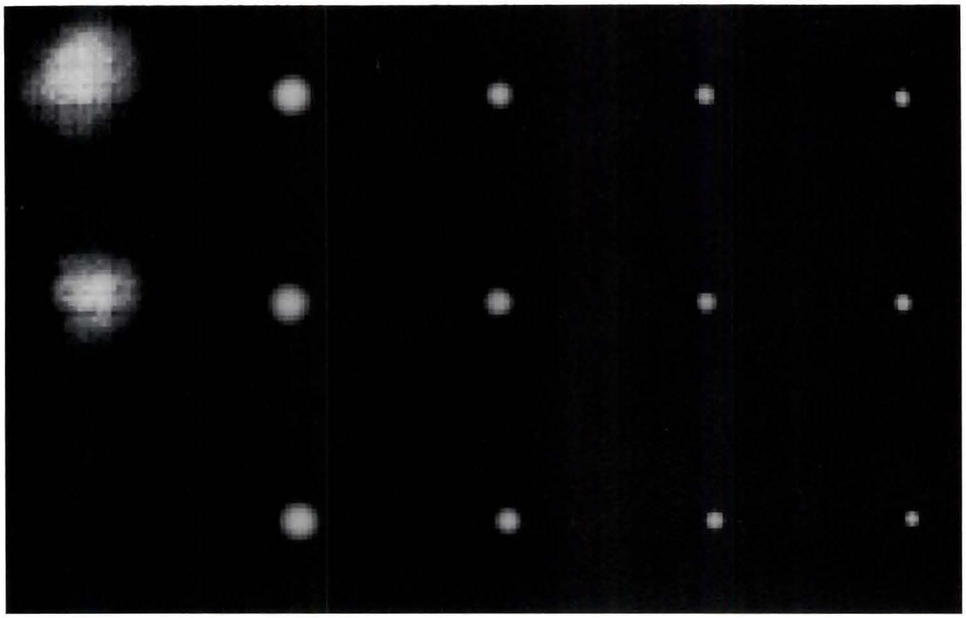

Fig. 14—Under conditions of high light level the resolution in the image reconstruction is not determined by the seeing but by the spatial filter in the processing algorithm. The lower row shows the result of processing a true point source (with no seeing effects) at each of the spatial-filter settings. The top row shows a time exposure of star 1 under average seeing condition (the left-most image) and the reconstructed images for each of the spatial-filter settings. The second row contains the same treatment for star 2 observed in good seeing.

sphere, determines the resolution limit. The reconstructed images of both stars approach the quality of the reference object or point source. Each of the two reconstructions combines 9,000 frames of 10-ms duration. With signal levels of approximately 45,000 detected photons/s, a total of 4 million photons produced each of the reconstructed images. Under these circumstances, with an adequate number of photons the speckle-imaging process overcomes atmospheric distortion and successfully reconstructs an image.

Star Observations (Signal-Level Dependence)

To compare star-image reconstruction with satellite-image reconstruction, shorter frame times and shorter total exposure times must be considered. Because of satellite motion, total exposure times for satellite imaging can be no longer than approximately 5 s. Figure 15 contains image reconstructions of star 2, with a frame time of 2 ms for each of the filter values 0.2, 0.3, 0.4, and 0.5 across the row. Images in the top row are the result of processing 2,500 frames of data, over an exposure time of 5 s. Images in the middle row are the result of 1,000 frames collected over 2 s, and images in the lower row are the result of 500 frames over 1 s. Figure 16 shows the results for star 1, obtained with the same parameters but under poorer seeing conditions. For both stars the 5-s exposures correspond to a total of 250,000 detected photons per image, the 2-s exposures correspond to 100,000 photons, and the 1-s exposures correspond to 50,000 photons. The image reconstructions for star 2 are above the general background noise level in all cases, even though the 1-s exposure example appears noisy. The poorer seeing for star 1 produces much poorer images. Thus the seeing quality determines how many photons are required to allow the satisfactory reconstruction of each point of light in the image. Indeed, these figures are a qualitative demonstration of the theoretical prediction that,

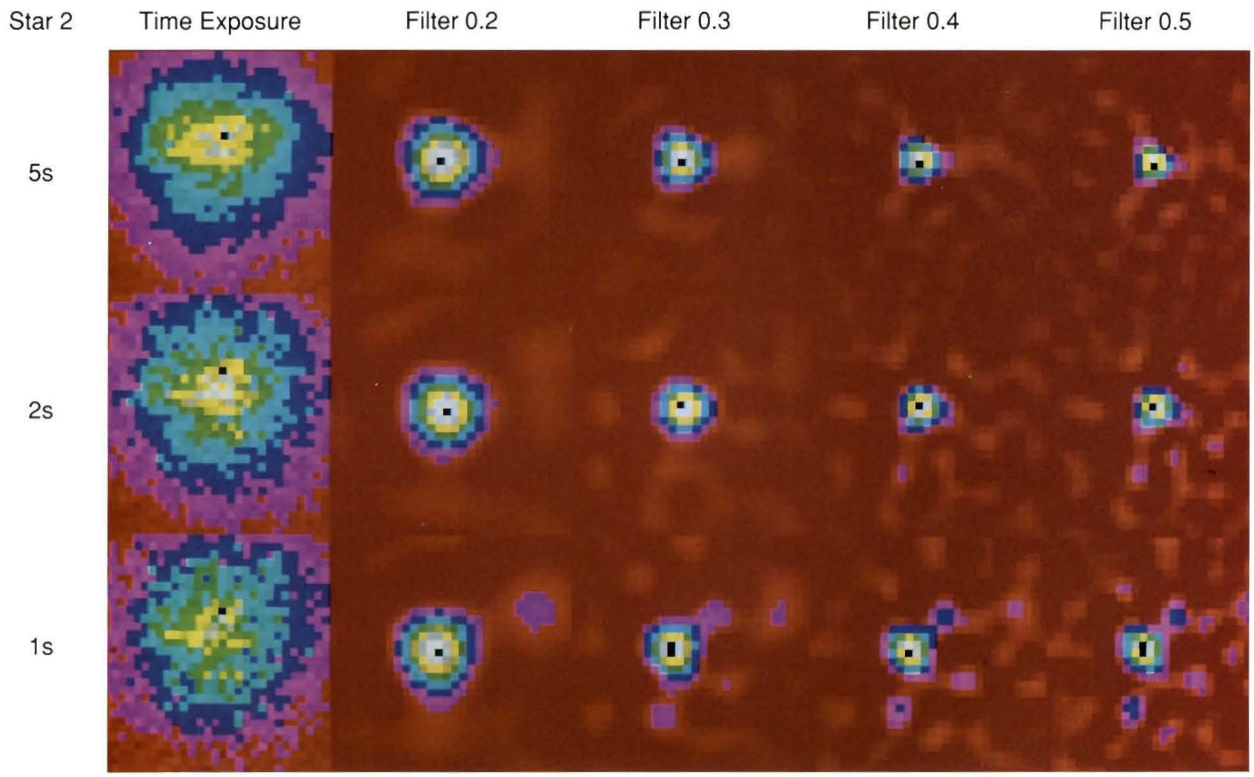

Fig. 15—Signal-level dependence is investigated by reducing the portion of the data sample employed in the reconstruction of images of star 2 in good seeing. The top row, middle row, and lower row result from data intervals of 5 s, 2 s, and 1 s, respectively.

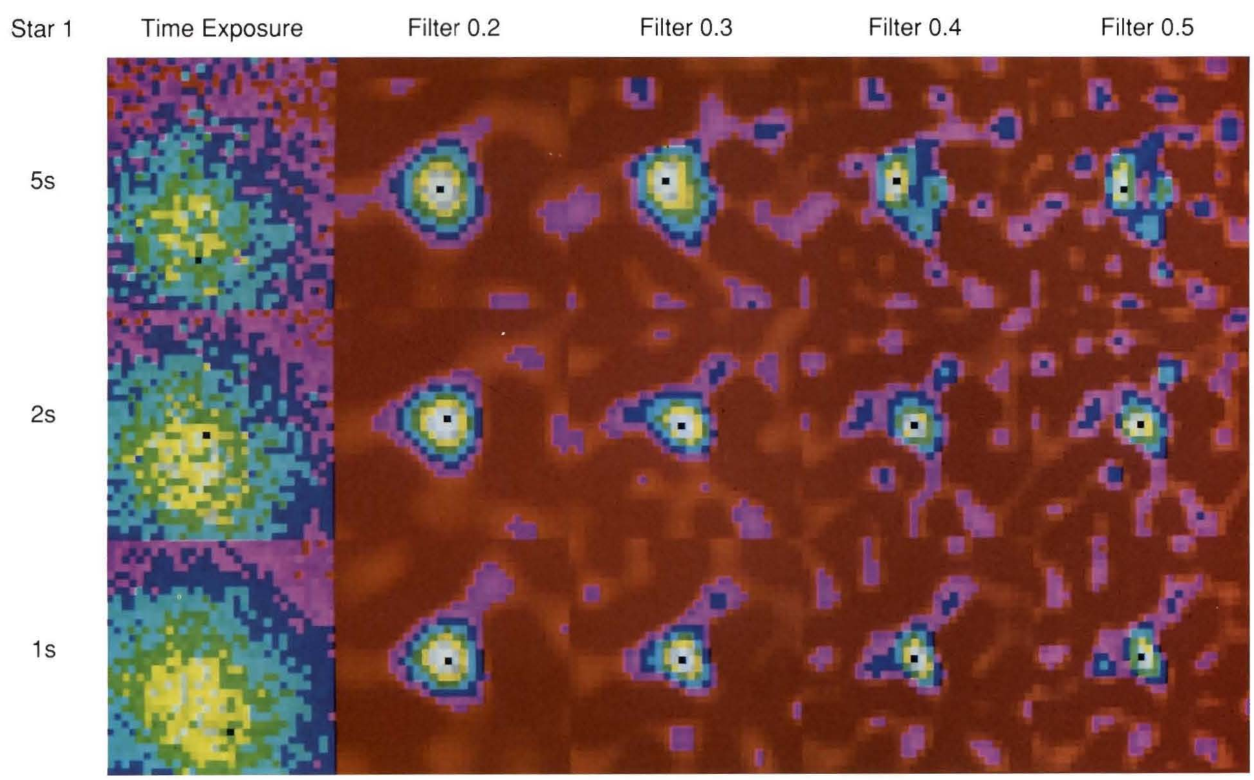

Fig. 16—Same as Fig. 15, but for the case of star 1 in average seeing.

all else being equal, the number of frames required for successful image reconstruction $\approx (1/r_0^4)$ [6]. When seeing conditions are like those for star 2, at least 50,000 detected photons are required for the successful reconstruction of each light center in any object in these experiments.

Satellite Observations

To apply the reconstruction technique to satellite observations, it was necessary to find a suitable telescope. With the cooperation of the Laser Radar Measurements Group at Lincoln Laboratory, an observing run was scheduled and performed on the Firepond 1.2-m telescope early in 1988.

The observing run provided an excellent opportunity to obtain speckle-image data for numerous near-earth satellites during periods just after evening twilight and just before morning twilight. The rapid transit of these objects across the sky allows, in most cases, about three minutes of favorable observing at elevations above 50°. Typical satellite brightnesses range from third visual magnitude to seventh visual magnitude, depending on size; many satellites reach peak brightness near the highest part of the pass. Some satellites show rapid brightness variations that indicate rapid rotation. In general, satellites passing within about 1,000 km of the telescope provide sufficient signal for the speckle-imaging process.

The data were processed with various intervals for the frame time. A 2-ms frame time was sufficiently short, but in some cases times as long as 5 ms were selected without significant degradation of image quality. In the configuration used for the first experiments, mirrors directed the optical beam to the PAPA detector at a fixed position off the telescope (i.e., a coudé, configuration). The primary disadvantage of such a configuration is that the telescope elevation and azimuth motions cause the image to rotate on the face of the detector during the pass. It was possible, however, to remove the blurring due to rotation by removing the rotation from each frame in the data set prior to the speckle processing. Such procedures allow the use of frame times up to 5 s to produce a single satellite image.

The Firepond experiments demonstrate that speckle imaging of satellites in near-earth orbits can be achieved despite the additional measurement difficulties that satellite motion created. The quality of the images depends strongly on how many photons can be detected in each frame, and how many frames can be combined to produce a single image. In the first speckle-imaging experiments reported here, a relatively low-sensitivity detector was used. Under these circumstances the spatial filter in the reconstruction algorithm determines the resolution limit. With better detectors, resolution approaching the predicted limit for the telescope should be possible.

The Role of Speckle Imaging

Speckle imaging is an alternative optical technique for achieving high resolution in satellite applications. The speckle technique employs simple, rugged, and comparatively inexpensive equipment, in contrast to the complex electro-optical configuration needed for successful adaptive-optics applications. The optimal spectral bandwidth $\Delta\lambda$ for the speckle method is relatively narrow, and is set by the telescope diameter D and the seeing scale r_0, for $\lambda = 6{,}500$ Å, according to Ref. 17:

$$\Delta\lambda \le 2{,}900 \text{ Å} \cdot (r_0/D)^{5/6}.$$

The bandwidth for the measurements reported in this article was 350 Å. Although in adaptive optics no corresponding bandwidth limitation exists, much of the available light must be used to determine the compensating distortion of the mirror surface. Therefore, brighter sources are required despite the bandwidth advantage.

Although the speckle-imaging application reported in this paper involves only a single telescope with a single objective mirror, the reconstruction method also has immediate applicability to other more complicated and potentially useful optical systems. For example, the PAPA detector and bispectrum-processing procedures can be applied to the detection and reconstruction of images produced by a cophased array of multiple mirrors, or other interferometer configurations. This application is especially important for achieving the large effective apertures needed for some satellite observations. Another attractive possibility is to place the detector in the focal plane of a compensated mirror or adaptive-optics system to see if the speckle image-reconstruction process can further improve the adaptive-optics image quality.

The speckle method requires considerable computation by a workstation computer after the collection of frames. If swifter results are desired, a specially designed processor could perform the image reconstruction. As the reconstruction algorithms improve, a corresponding improvement can also be made in any data base of images from earlier processing procedures. Thus the simplicity, low cost, portability, and ease of application of the speckle-imaging technique make it a valuable addition to techniques for monitoring the near-earth environment.

Acknowledgments

The authors express their appreciation to Professor Costas Papaliolios of Harvard University for his cooperation and participation in this project. We thank him and his colleagues for the use of the PAPA camera and laboratory facilities for tests of the camera, which made the reported experiments possible. We are especially indebted to Leo Sullivan, James Daley, Lawrence Swezey, Raymond Capes, Jr., and Michael Mattei for their enthusiastic participation in the Firepond experiments. We thank Ramaswamy Sridharan, Richard Lacoss, Gerald Banner, and Antonio Pensa for their encouragement in this effort, and their cooperation in creating the environment appropriate for such a project. James Beletic was a guest observer at Las Campanas Observatory in collaboration with Professor Richard Goody of Harvard University. The Las Campanas Observatory is operated by the Carnegie Institution. This work was sponsored by the Department of the Air Force.

References

1. F. Roddier, "Triple Correlation as a Phase Closure Technique," *Opt. Commun.* **60,** 145 (1986).
2. C. Higgs, E.D. Ariel, B.E. Player, and L.C. Bradley, III, "Adaptive-Optics Compensation through a High-Gain Raman Amplifier," *Lincoln Laboratory Journal* **2,** 105 (1989).
3. A. Labeyrie, "Attainment of Diffraction-Limited Resolution in Large Telescopes by Fourier Analysing Speckle Patterns in Star Images," *Astron. Astrophys.* **6,** 85 (1970).
4. H.A. McAlister, "High Angular Resolution Measurements of Stellar Properties," *Annu. Rev. Astron. Astrophys.* **23,** 59 (1985).
5. J.C. Dainty and J.R. Fienup, "Phase Retrieval and Image Reconstruction for Astronomy," *Image Recovery: Theory and Application*, ed. Henry Stark (Academic Press, London, 1987), p. 231.
6. K.T. Knox and B.J. Thompson, "Recovery of Images from Atmospherically Degraded Short-Exposure Images," *Astrophys. J.* **193,** L45 (1974).
7. P. Nisenson and C. Papaliolios, "Effects of Photon Noise on Speckle Image Reconstruction with the Knox-Thompson Algorithm," *Opt. Commun.* **47,** 91 (1983).
8. G. Weigelt, "Modified Astronomical Speckle Interferometry 'Speckle Masking,'" *Opt. Commun.* **21,** 55 (1977).
9. A.C.S. Readhead, T.S. Nakajima, T.J. Pearson, G. Neugebauer, J.B. Oke, and W.L.W. Sargent, "Diffraction-Limited Imaging with Ground-Based Optical Telescopes," *Astron. J.* **95,** 1278 (1988).
10. J.W. Goodman and J.F. Belsher, "Fundamental Limitations in Linear Invariant Restoration of Atmospherically Degraded Images," *SPIE* **75**: *Imaging through the Atmosphere*, p. 141 (1976).
11. B. Wirnitzer, "Bispectral Analysis at Low Light Levels and Astronomical Speckle Masking," *J. Opt. Soc. Am.* **2**, 14 (1985).
12. C. Papaliolios, P. Nisenson, and S. Ebstein, "Speckle Imaging with the PAPA Detector," *Applied Optics* **24**, 287 (1985).
13. S. Ebstein, "Signal-to-Noise in Photon-Counting Speckle Interferometry with Real Detectors," *Digest of Topical Meeting on Quantum-Limited Imaging and Image Processing* (Optical Society of America, Washington, 1986), p. 32.
14. C.L. Nikias and M.R. Raghuveer, "Bispectrum Estimation: A Digital Signal Processing Framework," *Proc. IEEE* **75**, 869 (1987).
15. J.W. Christy and R.S. Harrington, "The Satellite of Pluto," *Astron. J.* **83,** 1005 (1978).
16. J.W. Beletic, R.M. Goody, and D.J. Tholen, "Orbital Elements of Charon from Speckle Interferometry," *Icarus* **79**, 38 (1989).
17. F. Roddier, "Atmospheric Limitations to High Angular Resolution Imaging," *Proc. of ESO Conf. on Scientific Importance of High Angular Resolution at Infared and Optical Wavelengths, Garching, 24 March 1981*, p. 5.

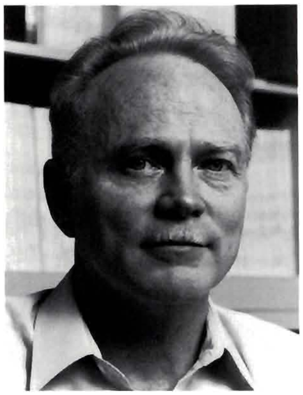

WILLET BEAVERS is a staff member in the Surveillance Techniques Group. He joined Lincoln Laboratory in 1986 after 21 years at Iowa State University, where he was a professor of astrophysics. At ISU his research interests included observations and experiments in stellar interferometry, spectrometry, lunar occultations, observatory instrument development, and stellar radial-velocity measurement. He accumulated over 17 minutes of totality while taking teams on solar eclipse expeditions to Indonesia, Canada, India, and Africa. Willet has B.S. and M.S. degrees in physics from the University of Missouri, and a Ph.D. degree in astrophysics from Indiana University. He also served as a gunnery officer aboard a small combatant vessel during a tour in the U.S. Navy. Since he joined the Laboratory, his work has primarily been concerned with utilizing optical instruments and techniques in space surveillance applications.

DAN E. DUDGEON is an assistant leader of the Machine Intelligence Technology Group. His research specialities are in image processing, computer vision, and computer architectures for algorithm development and real-time implementations. Before joining Lincoln Laboratory in 1979, he worked at Bolt, Beranek, and Newman, Inc. in Cambridge, Mass. Dan received his S.B., S.M., and E.E. degrees in electrical engineering, and his Sc.D. degree in signal processing, all from MIT. In 1976 he was corecipient of IEEE's Browder J. Thompson Memorial Prize for best paper by an author under the age of 30. He is the coauthor of *Multidimensional Digital Signal Processing*; he is a charter member and past chairman of the IEEE Acoustics, Speech, and Signal Processing Society's Technical Committee on Multidimensional Signal Processing; and he is currently serving as secretary of the ASSP Society Administrative Committee. Dan was elected an IEEE Fellow in 1987, and he was named a Distinguished Lecturer of the ASSP Society in 1988.

JAMES W. BELETIC is a staff member in the Surveillance Techniques Group. He received a B.S. degree in physics from Fairfield University, and an S.M. and a Ph.D. degree in applied physics from Harvard University. Jim previously worked in the sensor technology division of The Analytic Sciences Corporation. His research speciality is speckle imaging.

MARK T. LANE is a staff member in the Surveillance Techniques Group, where his speciality is orbital dynamics and metric data analysis. Before joining Lincoln Laboratory in 1986, he was an instructor of mathematics at Auburn University. Mark received bachelor degrees in both music and mathematics from Western Kentucky University, and M.S. and Ph.D. degrees in mathematics from Vanderbilt University.